Improved Performance of Direct-Drive Implosions with a Laser-Shaped Adiabat

Introduction

The minimum energy required for ignition of the imploding capsule in inertial confinement fusion is a strong function of the fuel adiabat (the ratio of the shell pressure to the Fermi-degenerate pressure) α_{stag} at the time of maximum compression: $E_{\min} \sim \alpha_{\text{stag}}^3$. Thus, to minimize the energy, the shell must be driven on the lowest possible adiabat. The performance of low-adiabat implosions is limited by hydrodynamic instabilities that tend to disrupt the shell during the acceleration phase. The most important instability is the Rayleigh–Taylor[1,2] (RT) instability seeded by single-beam nonuniformities and surface roughness. The main mechanism that reduces the RT growth is mass ablation from the target surface,[3] characterized by the ablation velocity V_a. The ablation velocity, in turn, increases with the adiabat α in the ablation region as $V_a \propto \alpha^{3/5}$. As the shell accelerates, the RT instability takes place at the outer part of the shell, which ablates during the implosion. Thus, one can satisfy the requirements of the lower-adiabat fuel at the maximum compression and the higher-adiabat ablation region by shaping the adiabat inside the shell.

Experiments have been done in both planar[4–8] and convergent[9,10] geometries to understand the evolution of perturbations at the ablation surface during acceleration of a planar foil or implosion of a cylinder or hemisphere. The ablation surface and the shell–fuel surface are coupled in that perturbations on the shell–fuel interface can "feed out"[11] to the ablation surface and perturbations that grow on the ablation surface can "feed through"[12] to the shell–fuel interface.

Interface perturbations grow exponentially $\left(a = a_0\, e^{\gamma t}\right)$ during the "linear" phase of the RT instability and reach a saturation phase (when $a \sim \lambda/10$) where the growth continues at a reduced rate.[13] Here, a is the amplitude of the perturbation, a_0 is the initial perturbation amplitude (the seed), γ is the growth rate, and λ is the wavelength of the perturbation.

A great deal of effort has gone into reducing the seeds (a_0) due to illumination nonuniformities (imprinting) and target imperfections. The effect of imprinting has been reduced by a number of beam-smoothing techniques, including distributed phase plates (DPP's),[14] polarization smoothing (PS) with birefringent wedges,[15,16] smoothing by spectral dispersion (SSD),[17] and induced spatial incoherence (ISI).[18] The effect of the RT instability can also be reduced by lowering the RT growth rate. It has been shown that the ablation-surface RT growth rate is reduced by the ablation process.[3] Subsequent theoretical work that includes the effect of thermal transport[19] and experiments with planar targets[8] shows that the dispersion formula for a CH target is given by

$$\gamma = 0.98\sqrt{\frac{kg}{1+kL}} - 1.7 \cdot kv_a\,,$$

where k is the perturbation spatial wave number, g is acceleration, L is density scale length, and V_a is ablation velocity.

The ablation velocity term not only reduces the growth rate but stabilizes the interface for perturbation wavelengths shorter than the cutoff wavelength λ_c, where

$$\lambda_c = \frac{4\pi L}{\sqrt{1+4\left(\frac{0.98}{1.7}\right)^2 \times \frac{Lg}{V_a^2}}},$$

which, in the limit that $k \times L << 1$, is

$$\lambda_c = 2\pi\left(\frac{1.7}{0.98}\right)^2 \times \frac{V_a^2}{g}.$$

The ℓ mode of a perturbation on a spherical target is given approximately by the circumference of the target ($2\pi r$) divided by the perturbation wavelength, so that the cutoff ℓ mode $\ell_c \sim 2\pi r/\lambda_c$. A capsule is stable for modes equal to or larger than ℓ_c.

The ablation velocity is defined as the velocity at which the ablation surface moves into the target. This is given by the mass

ablation rate (the rate at which material is removed from the ablation surface) divided by the density of the same material. The mass ablation rate is determined by the intensity of the incident radiation onto the target; therefore, decreasing the density of material at the ablation surface can increase the ablation velocity.

Two techniques—radiation preheat[20] and driving a decaying shock wave[21]—have been proposed to decrease the density at the ablation surface by raising its temperature and causing the shell to decompress. Decreasing the density at the ablation surface increases the ablation velocity, the entropy of the ablation surface, and thus the adiabat. One must be careful, however, to increase the shell adiabat at the ablation surface only and not the whole shell or the fuel. The entropy of the fuel must be minimally affected by these techniques so that the target will continue to be compressed efficiently.

Adiabat Shaping in Spherical Implosions

An experiment was designed to test the technique of launching a decaying shock wave into a spherical shell, setting the adiabat of the shell high at the ablation surface and low at the fuel–shell interface. This was accomplished by adding a narrow picket pulse to the beginning of a laser pulse shape designed to implode a target with a low shell adiabat as shown by the thick solid curve of Fig. 91.13. The picket pulse initiates a shock wave in the shell that becomes unsupported in that the pressure at the ablation surface is decreased, resulting in the generation of a rarefaction wave the propagates toward the shock wave. The rarefaction wave overtakes the shock wave, and the resultant shock wave decays as it propagates through the shell. The laser-irradiation pulse shape is designed so that the shock wave affects the ablation interface with minimal change at the shell–fuel interface.

The experiment was designed around a D_2-filled polystyrene shell, 33 μm thick and 905 μm in diameter filled to a pressure of 15 atm. Two pulse shapes (shown in Fig. 91.13) were used to compress this shell with a low adiabat ($\alpha = 2$) at the fuel–shell interface. The main drive pulse, shown as the thin solid curve, has a 2-TW, 700-ps-long foot followed by a power law rise[22] to a peak intensity of 20 TW on target. The foot pulse drives a shock wave that is fully supported throughout the implosion and changes the entropy of the shell and fuel. The dotted curve in Fig. 91.13 shows an actual pulse shape used during the experiments.

The optimum picket pulse is one that will raise the adiabat of the ablation surface without affecting, or minimally affecting, the fuel–shell interface adiabat. It was found by one-dimensional (1-D) hydrodynamic simulations that this optimum pulse for the implosions with a picket pulse was comprised of a narrow, 100-ps-FWHM (full width at half maximum), Gaussian picket combined with the main drive pulse described above. This combined pulse, shown as the thick solid curve in Fig. 91.13, has a picket 750 ps before the half-maximum intensity point of the power-law rise of the drive pulse. The narrowest picket pulse available on OMEGA for these experiments had a FWHM of 120 ps. The experiment was designed with a pulse using a 120-ps picket placed at 340 ps before the half-maximum point of the compression pulse shown as the dashed curve in Fig. 91.13. The total laser energy on target is 19 kJ with 0.9 kJ in the picket pulse.

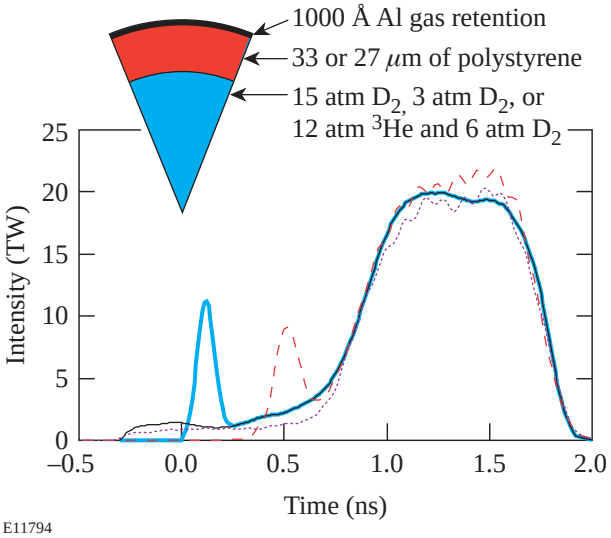

E11794

Figure 91.13
(Inset: Types of targets used to study the effect of a picket pulse on the implosion of a spherical gas-filled shell. Targets with either a 33-μm- or 27-μm-thick polystyrene shell were filled with either 15 atm of D_2, 3 atm of D_2, or a mixture of 12 atm of ^{3}He and 6 atm of D_2.) Pulse shape used to measure the effect of a picket pulse before a drive pulse on the performance of an implosion. The drive pulse was designed to implode a spherical cryogenic DT target on an isentrope. This pulse shape implodes a gas-filled CH shell as an $\alpha = 2$ isentrope. This pulse shape is shown as the thin solid curve (which is covered by the thick solid curve after 0.25 ns). The actual pulse shape delivered by the laser is shown as the dotted curve. The optimum picket pulse has an intensity of 55% of the drive pulse intensity, is 100 ps wide between the half-intensity points, and precedes the compression pulse by 750 ps. This pulse shape is shown as the thick solid curve. The actual picket was 120 ps wide so it had to be positioned 340 ps ahead of the drive pulse with an amplitude of 40% of the drive pulse. The actual picket and drive pulse combination used is shown as the dashed curve.

The effect of the picket on the implosions is shown in Figs. 91.14 and 91.15. Stability was calculated using the output from the 1-D hydrodynamics simulation code *LILAC*.[23] The calculation uses *LILAC* output to determine values for the shell's physical quantities, an assumed initial perturbation spectrum at the ablation surface, and a model for RT growth[12] to determine the amplitude of perturbations at the ablation surface during an implosion. The initial perturbation is a quadrature sum of the illumination nonuniformity as calculated by a two dimensional (2-D) hydrodynamics simulation and the measured target outer-surface roughness.[24] The amplitude of the inner peak, or bubble, of the perturbation divided by the shell thickness is shown in Fig. 91.14. It is assumed that the perturbation disrupts the shell when this value is equal to 1. For the case of the pulse shape without a picket (shown as the thick solid curve), this occurs at the peak of the compression pulse at 1.28 ns. The thin solid curve in Fig. 91.14 shows the result when a picket is added to the beginning of the compression pulse. The bubble-to-shell thickness ratio stays below 1 during the entire time that the laser irradiates the target, reaching a maximum value of 0.7 near the end of the compression pulse. This analysis indicates that the shell driven with a picket pulse is more stable during the acceleration phase of the implosion than one driven without a picket.

Figure 91.15 shows the simulated shell density and adiabat as functions of radius at the time of maximum acceleration for two separate implosions. Densities are plotted as solid curves,

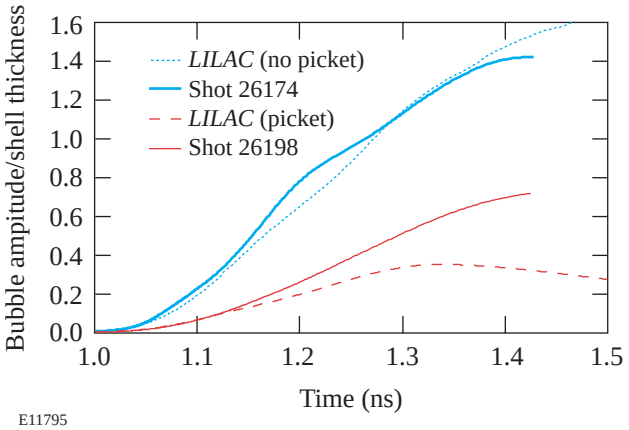

Figure 91.14
Bubble amplitude divided by the shell thickness calculated by a stability postprocessor applied to the output from the 1-D hydrodynamic simulation *LILAC*. The thick and dotted curves indicate the laser pulse without a picket. The thin and dashed curves indicate pulse shapes with a picket. The dashed and dotted curves indicate the ideal pulse shape for a 15-atm-D_2-filled, 33-μm-thick polystyrene shell. The thick and thin curves are calculated for the actual pulse shapes delivered onto the target.

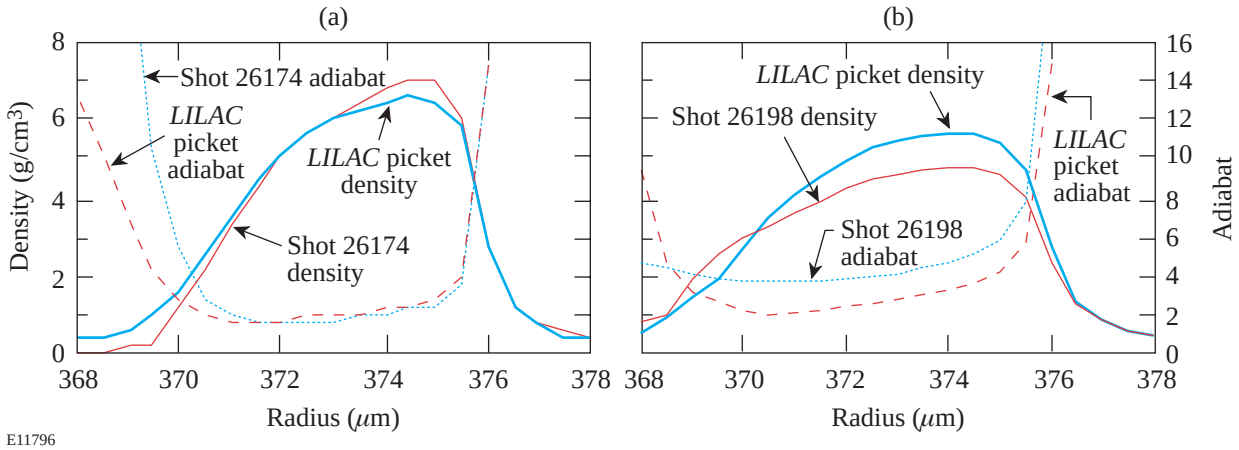

Figure 91.15
The density and adiabat versus position at the time of peak acceleration calculated from *LILAC*. In (a) with the drive pulse only, the density is plotted as solid lines, and the adiabat is plotted as broken lines. In (b) the density and adiabat are plotted with a picket pulse added to the compression pulse. The thick and dashed lines in both (a) and (b) are calculated from *LILAC* for the optimum laser pulse shapes. The thin and dotted lines are calculated for the pulse shape used in the experiment.

and the adiabats are plotted as dashed curves. Figure 91.15(a) shows the results for illumination without a picket for both the ideal and actual pulse shapes, and Fig. 91.15(b) shows the results for pulses with a picket, again for both the ideal and actual pulse shapes. The ablation surface is at the position of 376 μm, where the density is 2.5 g/cm^3. The value of the adiabat at the ablation surface without a picket is 3.9 and with a picket is 5.6. The fuel–shell interface is at a position of 372 μm for the pulse shape without a picket and 370 μm for illumination with a picket. The value of the adiabat is 1.7 for pulses without a picket and 2.1 for pulses with a picket.

Experimental Results

The OMEGA[25] laser system was used to implode spherical targets with the above pulse shapes. Sixty beams of 351-nm radiation were incident onto the target. All beams had polarization smoothing, 1-THz bandwidth, 2-D SSD, and DPP's with an intensity envelope given by a third-order super-Gaussian to minimize the illumination nonuniformities imposed by the laser. The targets used for these measurements are shown as the inset in Fig 91.13. The shells were made of polystyrene either 33 or 27 μm thick and filled with three gas-fill conditions: 15 atm of D_2; 3 atm of D_2; and a mixture of 12 atm of ^{3}He and 6 atm of D_2. All targets had a 1000-Å layer of aluminum to act as a gas-retention barrier. The laser pulse shapes were optimized for an outer diameter of 906 μm, and the delivered targets had diameters that ranged from 901 to 923 μm.

Both x-ray and fusion particle (neutron and proton) diagnostics were used to measure and quantify the implosions. X-ray framing cameras[26] were used to measure the time and spatially dependent x-ray emission during the implosion. X-ray microscopes[27] were used to study the final core spatial shapes. Neutron yields and spectra were measured with scintillator time-of-flight counters[28–30] at 3.5 and 7 m from the center of the target chamber. Protons from fusion processes were detected with range filters[31] designed to determine both their yield and energy spectrum.

It is important that the 1-D hydrodynamic simulation calculate the implosion dynamics correctly when a model is used to determine the growth of perturbations. Two x-ray framing cameras were used to measure the radius of the imploding shell as a function of time. The data for all 15-atm-gas-filled, 33-μm-thick CH shells are plotted in Fig. 91.16. These data are from 15-atm-D_2-filled and 12-atm-^{3}He/6-atm-D_2-filled targets. The experimental data are the value of the peak x-ray emission radius of a two-dimensional image and are plotted as crosses. The *LILAC*-calculated position of the outer and inner shell surfaces are plotted as solid and dashed lines. The inner and outer shell radii are determined by radii at which the density is 1/*e* times the peak density of the shell. Data for laser irradiation without the picket pulse are plotted in Fig. 91.16(a), and data for laser irradiation with the picket are plotted in Fig. 91.16(b). The *LILAC* calculations agree reasonably well with the experimental data. This indicates that the motion of the imploding target is calculated correctly.

X-ray images of the core emission from a Kirkpatrick–Baez (KB) microscope are shown in Fig. 91.17. These images are integrated in time; however, most of the x-ray emission from the core comes during the peak compression of the target. The image from an implosion without a picket pulse is shown in Fig. 91.17(a), and the image from an implosion with a picket pulse is shown in Fig. 91.17(b). The images show a more-intact fuel mass when a picket pulse is added to the main compres-

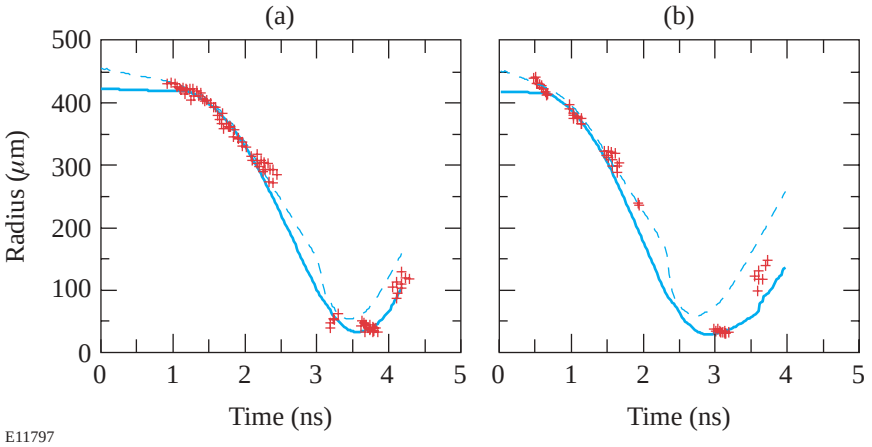

Figure 91.16
Radius versus time for all 15-atm-filled, 33-μm-thick CH shell targets. The plot in (a) shows data for laser irradiation using the compression pulse without a picket pulse. Averages for *LILAC*-calculated position of the inner and outer shell radius are plotted as solid and dashed lines, and the experimental data as measured with two x-ray framing cameras are plotted as crosses. The plot in (b) shows data taken with a picket pulse. The solid and dashed curves are averages of the *LILAC*-calculated positions of the inner and outer shell radius. The experimental data as measured with x-ray framing cameras are plotted as crosses.

sion pulse. Lineouts along the lines shown in the images are plotted in Fig. 91.17(c). The lineout of the image without a picket pulse is plotted as a dashed curve. Lineout data from the image with a picket pulse are plotted as the solid line. Figure 91.17(c) shows that the lineout from the implosion with a picket is typical of that from a "limb-brightened" image and shows that the implosion was more stable than the implosion without a picket.

Results from the fusion-product-yield measurements for three shots for each target and pulse shape are shown in Table 91.I. It can be seen from the data that for the 15-atm-D_2-filled, 33-μm-thick shell, there is a factor-of-3 increase in the number of 3-MeV neutrons from the target irradiated with a picket pulse than that from the target without a picket. The experiment was optimized for the 33-μm-thick shells; the improvement for the 27-μm-thick shells is only 50%. Both the 3-atm-D_2-filled and the ^{3}He-D_2-filled, 33-μm-thick shells show an improved fusion yield by a factor of 2. The ratio of the measured primary neutron yield to the neutron yield predicted by the hydrodynamics simulation [usually referred to as yield-over-clean (YOC)] for the 15-atm-D_2-filled, 33-μm-thick shells improves from 0.03 to 0.19. In all cases, the YOC can be seen to improve significantly.

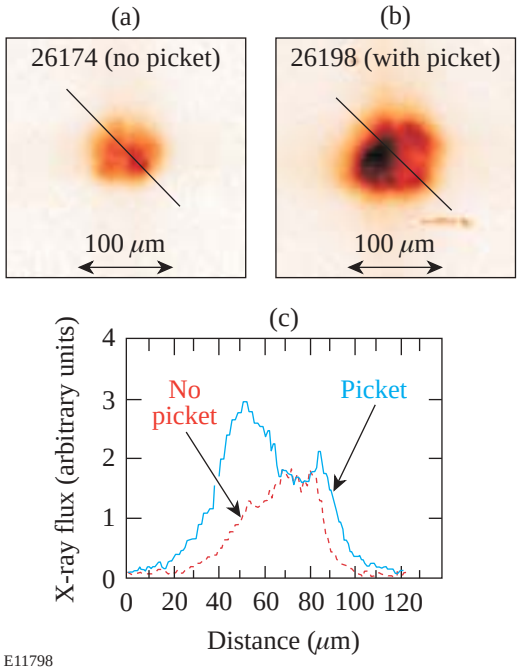

Figure 91.17
X-ray microscope images of target cores formed from a 33-μm-thick CH shell filled with 15 atm of D_2; (a) with only the main compression pulse used; (b) when a picket pulse was added to the compression pulse. Lineouts through the images are shown in (c). The dashed line is the lineout without a picket pulse; the solid line is the lineout with a picket pulse.

Table 91.I: Summary of fusion-product measurements and simulation output. The first column describes the composition, shell thickness (mm, in square brackets), and fill pressure (atm, in parentheses) of the target.

	Experimental Measurements			*LILAC* Simulation Output		
Target	Yield (D_2)	Yield (DT)	Yield (D^3He)	Yield (D_2)	Yield (DT)	Yield (D^3He)
Without picket						
D_2(15)CH[33]	4.14×10^9	7.99×10^6	2.96×10^6	1.17×10^{11}	3.04×10^8	1.66×10^8
D_2(3)CH[33]	1.06×10^9	8.00×10^5	1.83×10^6	4.17×10^{10}	9.51×10^7	6.34×10^7
^{3}He(12)D_2(6)CH[33]	9.32×10^8	9.30×10^5	2.94×10^6	1.54×10^{10}		
D_2(15)CH[27]	1.98×10^{10}	3.89×10^7	1.83×10^7	2.50×10^{11}	6.60×10^8	4.18×10^8
With picket						
D_2(15)CH[33]	1.27×10^{10}	3.57×10^7	7.26×10^6	6.60×10^{10}	1.20×10^8	8.12×10^7
D_2(3)CH[33]	1.98×10^9	1.83×10^6	1.88×10^6	1.19×10^{10}	1.36×10^7	1.15×10^7
^{3}He(12)D_2(6)CH[33]	1.44×10^9	1.77×10^6	5.75×10^6	8.20×10^9		
D_2(15)CH[27]	2.96×10^{10}	5.22×10^7	2.96×10^7	1.94×10^{11}	4.15×10^8	3.05×10^8

Neutron-production rates for the 15-atm-D_2-filled, 33-μm-thick shell, measured (open symbols) and predicted (solid curves), are shown in Fig. 91.18. The thin curve and open square plots are data from the implosion without a picket. The thick curve and open circle plots are from the matching implosion using a picket. The experimental data were measured with the "neutron temporal diagnostic" (NTD).[32] The temporal offsets needed to compare experimental and simulation data were determined by maximizing the cross-correlation of the drive portion of the pulse as a function of a temporal shift relative to the laser pulse without a picket. This aligned the leading edges of the main drive pulse for all of the data. It is assumed that the neutron production is determined by the compression of the target by the drive pulse. An additional time shift was introduced to align the position of the shock neutron production calculated by *LILAC* for shapes without and with the picket pulse. The experimental data and the output from hydrodynamic simulations were processed in this manner so that the timing could be compared for all data. The temporal error for the relative times of emission is estimated to be of the order of 30 ps. The measured neutron burn rate divided by the calculated neutron burn rate from *LILAC* is plotted in Fig. 91.19. The data from implosions without a picket are plotted as open squares, and the data from implosions with a picket are plotted as open circles. The ratio of burn rates peaks at 0.35 for implosions with a picket pulse, while the ratio without a picket pulse peaks at 0.2. The neutron-burn-rate ratios show that the duration of neutron emission is longer for implosions with a picket pulse. Comparing the experimental data with predictions indicates that the implosions using a picket not only attain higher absolute yields than the implosions without a picket, they also return, as was stated earlier, a larger fraction of the 1-D yield. This suggests more-stable implosions with less mix due to RT growth.

While the experimental results from the neutron diagnostics reported above are encouraging, results from several other diagnostics remain inconclusive. Ion temperatures, inferred from the broadening of the neutron spectra, were reported to be from 2.1 to 2.5±0.5 keV for the 33-μm-thick shells and from 2.6 to 2.8±0.5 keV for the 27-μm-thick shells. There were no appreciable differences between implosions using the laser pulses with or without the picket. Additionally, the downshift of the primary proton energy can be used to measure the total ρR of the target integrated over the time of proton emission. The measured mean energy for the compression yield was 11.3±2.0 MeV for the implosion without a picket and 11.6±1.8 MeV for the implosion with a picket. The total ρR for both of these targets was inferred to be 106±8 and 108±8 mg/cm^2, respectively.

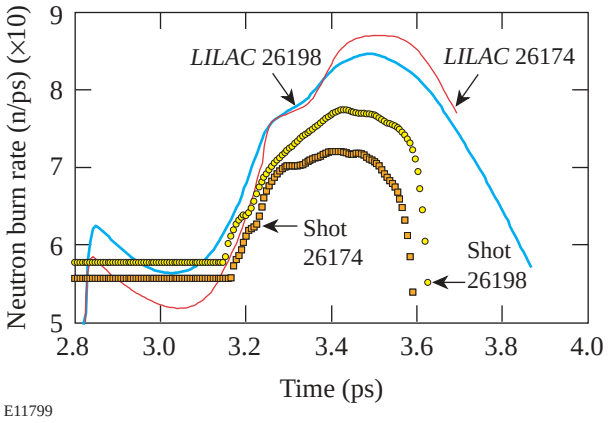

Figure 91.18
Neutron-production rates for a 15-atm-D_2-filled, 33-μm thick polystyrene shell. The thin curve and open squares are data for the pulse without a picket pulse. The thick curve and open circles are data for the pulse with a picket in front. Open symbols are the experimental measurements, and the solid curves are from the 1-D hydrodynamic simulation *LILAC*. Note that these points lie very close together before ~3.2 ns.

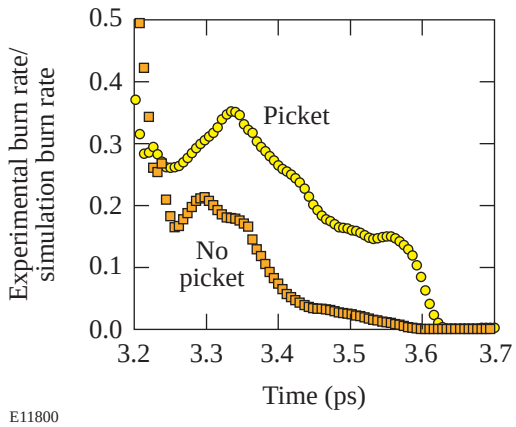

Figure 91.19
Experimental neutron-production rate divided by the neutron-production rate from a 1-D hydrodynamic simulation *LILAC* for a 15-atm-D_2-filled, 33-μm-thick polystyrene shell. The open square points are data for the pulse without a picket pulse, and the open circle points are data for the pulse with a picket in front.

Finally, results from the measurements of the 14.7-MeV proton emitted from the D^3He reaction are shown in Table 91.II. Targets filled with D^3He allowed for the measurement of the primary proton yield from the shock wave convergence at the center of the capsule. The mean energy for the protons was measured as 14.3 MeV for the laser irradiation both without and with a picket pulse. The number of protons from the shock wave is $7.1\pm1.2 \times 10^5$ without a picket pulse and $7.5\pm1.1 \times 10^5$ with a picket pulse as shown in column 2 of Table 91.II. Comparison of these measurements infer that the shock strength of the compression pulse is unaffected by the introduction of a picket. This would indicate that the shock created by a picket decayed in the shell before it had a chance to significantly alter the adiabat of the fuel.

Conclusion

An experiment has been performed to measure the effect of a picket pulse on the implosion of a spherical target. The purpose of this pulse was to initiate a decaying shock wave that lowers the density of the shell at the ablation interface but does not significantly affect the entropy of the shell–gas interface. The yields of fusion products are improved both in terms of the absolute value and in terms of the comparison to 1-D hydrodynamic simulation output. The increase in neutron yield for implosions with a picket pulse is not due to the added energy in the picket since both the absolute and relative neutron yields improved.

Between the two pulse shapes there is little change in either the total target ρR or the ion temperature. The neutron temperature measurement is the neutron-weighted ion temperature. It is possible this weighted measurement will be the same for both types of implosions. The ρR as measured with the protons from the D^3He reaction measures the total ρR of the target and not just the fuel ρR. This measurement is dominated by the thick target shells and is less sensitive to the fuel.

The emission rate for the 3-MeV neutrons compared to the simulation output shows that the start of emission calculated by the simulation compares well with the experimental data. The neutron-burn-rate measurements indicate that the 1-D simulation overestimates the duration of the neutron emission, probably due to the multidimensional effects not included in this type of calculation. The neutron emission from implosions using a picket pulse reaches a higher emission rate and a higher ratio of the experimental neutron burn rate to the *LILAC*-calculated neutron burn rate. Comparing the experimental data with predictions indicates that the implosions using a picket not only attain higher absolute yields than the implosions without a picket, they also return, as was stated earlier, a larger fraction of the 1-D yield. This demonstrates that picket pulses stabilize the implosion, resulting in less mix due to the RT growth at the ablation interface.

Table 91.II: Summary of 14-MeV proton measurements. The first column describes the target as in Table 91.I. The second column is the total number of protons emitted during the compression of the target. Column 3 is the number of protons emitted when the shock wave reaches the center of the target. The downshift of the protons is shown in column 4, and the calculated total ρR of the target is shown in column 5.

	Proton measurements			
Target	Yield (D^3He)	Yield (D^3He)	ΔE	ρR_{total}
Without picket	Compression	Shock	MeV	mg/cm^2
D_2(15)CH[33]	2.96×10^6		3.5±0.3	106±8
He^3(12)D2(6)CH[33]	2.94×10^6	7.11×10^5	3.4±0.3	104±8
D_2(15)CH[27]	1.83×10^7		2.6±0.2	81±6
With picket				
D_2(15)CH[33]	7.26×10^6		3.6±0.3	108±8
He^3(12)D2(6)CH[33]	5.75×10^6	7.51×10^5	3.5±0.2	106±6
D_2(15)CH[27]	2.96×10^7		3.0±0.2	92±6

ACKNOWLEDGMENT

This work was supported by the U.S. Department of Energy Office of Inertial Confinement Fusion under Cooperative Agreement No. DE-FC03-92SF19460 and the University of Rochester. The support of DOE does not constitute an endorsement by DOE of the views expressed in this article.

REFERENCES

1. Lord Rayleigh, Proc. London Math Soc. **XIV**, 170 (1883).
2. G. Taylor, Proc. R. Soc. London Ser. A **201**, 192 (1950).
3. S. E. Bodner, Phys. Rev. Lett. **33**, 761 (1974).
4. J. Grun *et al.*, Phys. Rev. Lett. **58**, 2672 (1987).
5. M. Desselberger *et al.*, Phys. Rev. Lett. **65**, 2997 (1990).
6. S. G. Glendinning, S. V. Weber, P. Bell, L. B. Da Silva, S. N. Dixit, M. A. Henesian, D. R. Kania, J. D. Kilkenny, H. T. Powell, R. J. Wallace, P. J. Wegner, J. P. Knauer, and C. P. Verdon, Phys. Rev. Lett. **69**, 1201 (1992).
7. C. J. Pawley *et al.*, Phys. Plasmas **6**, 565 (1999).
8. J. P. Knauer, R. Betti, D. K. Bradley, T. R. Boehly, T. J. B. Collins, V. N. Goncharov, P. W. McKenty, D. D. Meyerhofer, V. A. Smalyuk, C. P. Verdon, S. G. Glendinning, D. H. Kalantar, and R. G. Watt, Phys. Plasmas **7**, 338 (2000).
9. W. W. Hsing *et al.*, Phys. Plasmas **4**, 1832 (1997).
10. C. Cherfils *et al.*, Phys. Rev. Lett. **83**, 5507 (1999).
11. R. Betti, V. Lobatchev, and R. L. McCrory, Phys. Rev. Lett. **81**, 5560 (1998).
12. V. N. Goncharov, P. McKenty, S. Skupsky, R. Betti, R. L. McCrory, and C. Cherfils-Clérouin, Phys. Plasmas **7**, 5118 (2000).
13. S. W. Haan, Phys. Rev. A **39**, 5812 (1989).
14. T. J. Kessler, Y. Lin, J. J. Armstrong, and B. Velazquez, in *Laser Coherence Control: Technology and Applications*, edited by H. T. Powell and T. J. Kessler (SPIE, Bellingham, WA, 1993), Vol. 1870, pp. 95–104.
15. Y. Kato, unpublished notes from work at LLE, 1984.
16. T. R. Boehly, V. A. Smalyuk, D. D. Meyerhofer, J. P. Knauer, D. K. Bradley, R. S. Craxton, M. J. Guardalben, S. Skupsky, and T. J. Kessler, J. Appl. Phys. **85**, 3444 (1999).
17. S. Skupsky, R. W. Short, T. Kessler, R. S. Craxton, S. Letzring, and J. M. Soures, J. Appl. Phys. **66**, 3456 (1989).
18. R. H. Lehmberg and S. P. Obenschain, Opt. Commun. **46**, 27 (1983).
19. R. Betti, V. N. Goncharov, R. L. McCrory, P. Sorotokin, and C. P. Verdon, Phys. Plasmas **3**, 2122 (1996).
20. D. G. Colombant *et al.*, Phys. Plasmas **7**, 2046 (2000).
21. J. D. Lindl and W. C. Mead, Phys. Rev. Lett. **34**, 1273 (1975).
22. R. E. Kidder, Nucl. Fusion **16**, 3 (1976).
23. M. C. Richardson, P. W. McKenty, F. J. Marshall, C. P. Verdon, J. M. Soures, R. L. McCrory, O. Barnouin, R. S. Craxton, J. Delettrez, R. L. Hutchison, P. A. Jaanimagi, R. Keck, T. Kessler, H. Kim, S. A. Letzring, D. M. Roback, W. Seka, S. Skupsky, B. Yaakobi, S. M. Lane, and S. Prussin, in *Laser Interaction and Related Plasma Phenomena*, edited by H. Hora and G. H. Miley (Plenum Publishing, New York, 1986), Vol. 7, pp. 421–448.
24. P. W. McKenty, V. N. Goncharov, R. P. J. Town, S. Skupsky, R. Betti, and R. L. McCrory, Phys. Plasmas **8**, 2315 (2001).
25. T. R. Boehly, D. L. Brown, R. S. Craxton, R. L. Keck, J. P. Knauer, J. H. Kelly, T. J. Kessler, S. A. Kumpan, S. J. Loucks, S. A. Letzring, F. J. Marshall, R. L. McCrory, S. F. B. Morse, W. Seka, J. M. Soures, and C. P. Verdon, Opt. Commun. **133**, 495 (1997).
26. O. L. Landen *et al.*, in *Ultrahigh- and High-Speed Photography, Videography, and Photonics '93*, edited by P. W. Roehrenbeck (SPIE, Bellingham, WA, 1993), Vol. 2002, pp. 2–13.
27. F. J. Marshall and Q. Su, Rev. Sci. Instrum. **66**, 725 (1995).
28. T. J. Murphy *et al.*, Rev. Sci. Instrum. **66**, 930 (1995).
29. R. A. Lerche and T. J. Murphy, Rev. Sci. Instrum. **63**, 4880 (1992).
30. V. Yu. Glebov, D. D. Meyerhofer, C. Stoeckl, and J. D. Zuegel, Rev. Sci. Instrum. **72**, 824 (2001).
31. F. H. Séguin, C. K. Li, D. G. Hicks, J. A. Frenje, K. M. Green, R. D. Petrasso, J. M. Soures, D. D. Meyerhofer, V. Yu. Glebov, C. Stoeckl, P. B. Radha, S. Roberts, C. Sorce, T. C. Sangster, M. D. Cable, S. Padalino, and K. Fletcher, Phys. Plasmas **9**, 2725 (2002).
32. R. A. Lerche, D. W. Phillion, and G. L. Tietbohl, Rev. Sci. Instrum. **66**, 933 (1995).